RESEARCH ARTICLE

In Situ Synthesis of Molybdenum Carbide Nanoparticles Incorporated into Laser-Patterned Nitrogen-Doped Carbon for Room Temperature VOC Sensing

Huize Wang, Simon Delacroix, Anna Zieleniewska, Jing Hou, Nadezda V. Tarakina, Daniel Cruz, Iver Lauermann, Andrew J. Ferguson, Jeffrey L. Blackburn, and Volker Strauss*

Carbon laser-patterning (CLaP) is emerging as a new tool for the precise and selective synthesis of functional carbon-based materials for on-chip applications. The aim of this work is to demonstrate the applicability of laser-patterned nitrogen-doped carbon (LP-NC) for resistive gas-sensing applications. Films of pre-carbonized organic nanoparticles on polyethylenetherephthalate are carbonized with a CO_2-laser. Upon laser-irradiation a compositional and morphological gradient in the films is generated with a carbon content of 92% near the top surface. The specific surface areas of the LP-NC are increased by introducing sodium iodide (NaI) as a porogen. Electronic conductivity and surface area measurements corroborate the deeper penetration of the laser-energy into the film in the presence of NaI. Furthermore, impregnation of LP-NC with MoC_{1-x} (<10 nm) nanoparticles is achieved by addition of ammonium heptamolybdate into the precursor film. The resulting doping-sensitive nano-grain boundaries between p-type carbon and metallic MoC_{1-x} lead to an improvement of the volatile organic compounds sensing response of $\Delta R/R_0 = -3.7\%$ or -0.8% for 1250 ppm acetone or 900 ppm toluene at room temperature, respectively, which is competitive with carbon-based sensor materials. Further advances in sensitivity and in situ functionalization are expected to make CLaP a useful method for printing selective sensor arrays.

1. Introduction

Chemical sensors are gaining importance in everyday life for the detection and monitoring of pollutants, emissions, or sensing of biomarkers.[1] But also in view of the advent of future technologies in bionics and robotics we observe a rising demand for sophisticated chemical sensing architectures.[2] For practical applications and everyday use, ideal sensor materials are small, flexible, non-toxic, inexpensive, simple to produce, biodegradable, and operable at room temperature.[3] However, producing efficient sensors for the selective recognition of gaseous or liquid analytes is often a challenge because existing technologies and materials are complex and expensive.[4] Therefore, new production techniques and/or new materials and composites fulfilling all those requirements are needed.[5] Chemical sensor arrays are one possible solution for achieving high selectivity in analyte mixtures,[6] where the array selectivity is realized by pattern recognition using groups of individual sensors.[7]

H. Wang, S. Delacroix, J. Hou, N. V. Tarakina, V. Strauss
Max Planck Institute of Colloids and Interfaces
Am Mühlenberg 1, 14476 Potsdam, Germany
E-mail: volker.strauss@mpikg.mpg.de
S. Delacroix
LPICM
CNRS UMR 7647
Ecole polytechnique
Institut Polytechnique de Paris
Palaiseau 91128, France

A. Zieleniewska, A. J. Ferguson, J. L. Blackburn
National Renewable Energy Laboratory
Golden, CO 80401, USA
D. Cruz
Department of Inorganic Chemistry
Fritz-Haber-Institut der Max-Planck-Gesellschaft
Faradayweg 4-6, 14195 Berlin, Germany
D. Cruz
Department of Heterogeneous Reactions
Max Planck Institute for Chemical Energy Conversion
Stiftstraße 34-36, 45470 Mülheim an der Ruhr, Germany
I. Lauermann
PVcomB/Helmholtz-Zentrum Berlin für Materialien und Energie GmbH
Schwarzschildstraße 3, 12489 Berlin, Germany

**ADVANCED
SCIENCE NEWS**
www.advancedsciencenews.com

**ADVANCED
FUNCTIONAL
MATERIALS**
www.afm-journal.de

This is a particularly good solution to tackle unwanted effects, such as cross-interference of analytes at ambient conditions.[6] Simple and fast processing techniques with wide opportunities for chemical adjustments are required for the cost-effective realization of such chemical sensor arrays.

Laser-patterning of materials provides a solution for the direct synthesis of sensing materials for on-chip applications. In the past decade, laser-patterned carbons (LP-C) have emerged as versatile materials for sensor platforms with high surface areas and high binding affinities to a broad palette of compounds.[8] Commonly, LP-Cs or specifically laser-induced graphenes (LIG), are obtained by laser-irradiation onto films of polymeric precursor materials, such as graphene oxide[9,10] or polyimides.[11,12] Thereby, precisely printed electronically conductive carbon electrodes with high specific surface areas (SSA) on flexible substrates are obtained. Recently, we investigated this laser-patterning technique and developed a method to utilize simple and naturally abundant molecular compounds as starting materials.[13,14] These can be cast on flexible substrates and carbonized with a CO_2-laser to give 2D-patterns of electronically conductive nitrogen-doped carbons (NC), which show remarkable environmental stability.[15] Such NCs are commonly obtained from direct pyrolysis of nitrogen-containing precursors and show superior sorption properties.[16,17] In contrast, the so-called carbon laser-patterning (CLaP) process is an extremely cost-effective and fast method to produce NC-based platforms for chemical sensing.[18] Furthermore, CLaP enables simple modification with different types of functionalities or nanoparticles that can be incorporated into the LP-NC network.[13] The electronic and chemical modifications of these LP-NC networks facilitate the tuning toward higher sensitivity for certain analytes using, for example, metal carbides and inorganic salts.[19]

Metal carbides are well known for their high electronic conductivity, thermal stability, and corrosion resistance.[20] These attributes raise the interest in metal carbides as active materials in electronic and catalytic devices.[21,22] Due to their similar band-structure to noble metals, metal carbides are often ascribed great potential to replace the former as catalysts.[23,24] Their catalytic activity also makes metal carbides interesting for sensing applications.[19,25,26] However, in pure form, metal carbides suffer from low SSA, which is a drawback for sensing applications. Moreover, due to high hardness their films tend to crack or delaminate from the substrates.[27]

In particular, molybdenum carbides (Mo_2C or MoC) have been widely studied and are commonly used as electrocatalysts for biomass degradation or water splitting.[23,28] Molybdenum carbides are usually synthesized during pyrolysis in presence of a carbon source.[23] A great challenge is to increase their SSA by nano-structuring. For example, nanoparticles with sizes between 10 and 30 nm were achieved via the urea glass route.[29] However, the formation of small, high surface-area molybdenum carbide nanoparticles is mostly achieved in conjunction with electronically active support materials, such as metallic or metal oxide supports but also conductive NCs or carbon nitrides.[30,31] In synergy, NCs and nanocrystalline molybdenum carbides are expected to contribute their full performance toward improved interaction with adsorbates.[32]

In this study, we use CLaP to synthesize high-surface area NC-network supported MoC_{1-x} nanoparticles as chemiresistors for sensing volatile organic compounds (VOCs). The SSA of the LP-NC was increased by addition of sodium iodide (NaI) as an IR-laser transparent porogen. The final LP-NC films were characterized by X-ray powder diffraction, high-resolution scanning and transmission electron microscopy (TEM), energy dispersive X-ray spectroscopy (EDXS), and X-ray photoelectron spectroscopy (XPS) confirming the formation of the MoC_{1-x}-NC composite. Finally, defined resistive sensing platforms, printed on polyethylenetherephthalate (PET), and their performance to sensing VOCs such as acetone, toluene, and hexane at different atmospheric contents were tested. Pure carbon materials usually have no or a rather low room temperature response to non-redox VOCs, such as acetone or alcohols. In composites, positive effects of carbons, such as graphene or carbon nanotubes, added in low percentages are increased conductivity and surface areas.[33–35] We show that carbon with only 13 wt% molybdenum is the active sensing material and outperforms other carbon materials in terms of resistive response. These results lay a foundation for examining sorption-sensitive and potentially selective LP-NC based composites for the use in printed sensor arrays.

2. Experimental Section

2.1. Chemicals

Citric acid (99%, Sigma Aldrich), urea (>99.3%, Alfa Aesar), ammonium heptamolybdate tetrahydrate (≥99% for analysis, Acros Organics), ethylene glycol (≥99.7%, AnalaR Normapur, VWR chemicals), polyvinylpyrrolidone (PVP; average mol wt. 10 000, Sigma Aldrich), acetone (≥99.8% HPLC grade, Thermo Fisher Scientific GmbH), hexane (AnalaR Normapur, VWR chemicals), and toluene (≥99.8% HPLC grade, Thermo Fisher Scientific GmbH) were used as received.

2.2. Substrates

Silicon wafers were obtained from MicroChemicals. Wafers used were either 4-inch boron doped FZ-Si wafer, orientation (100), with a thickness of 0.5 mm and a generic resistivity of 3–100 kΩcm or 4-inch FZ-Si wafer, orientation (100), with a thickness of 0.5 mm and a generic resistivity of 10–1000 kΩcm. Aluminum foil used was 35 μm thick. The PET substrates were Melinex sheets obtained from Plano GmbH.

2.3. Preparation of the CNFA

The CNFA was prepared according to a previously published protocol.[15] In brief: citric acid and urea were annealed at 300 °C in a chamber oven for 2 h. After annealing, the black reaction product was dispersed in deionized H_2O and stirred at 95 °C for 24 h. The dispersion was centrifuged to obtain a black precipitate and a brown supernatant. The supernatant was removed and the washing process was repeated four times. After the last washing step, the precipitate was dried to obtain CA/U(300).

2.4. Preparation of the Precursor Films

PVP (film-forming agent; FFA) was dissolved in ethylene glycol (EtGly) to obtain a 0.2 g mL^{-1} solution (PVP/EtGly). Ammonium heptamolybdate (AHM; $(NH_4)_6Mo_7O_{24}$; 0.1 g·mL^{-1}) and/or sodium iodide (NaI; 0.1–0.4 g·mL^{-1}) were added and carefully dissolved. CA/U(300) was then added and stirred for 24 h to obtain a 0.8 g·mL^{-1} ink. All concentrations are given with respect to the volume of the solvent. A drop of the ink was applied onto the substrate and the ink was doctor bladed with a wet-thickness between 155 and 305 µm. Ethylene glycol was then evaporated at 80 °C on a precision hotplate (PZ2860-SR, Gestigkeit GmbH) to obtain the final films with thicknesses between 13 and 70 µm. The thickness was determined with a digital micrometer or cross-sectional SEM.

2.5. Laser-Carbonization

Laser-carbonization was conducted with a high-precision laser engraver setup (Speedy 100, Trotec) equipped with a 60 W CO$_2$ laser. Focusing was achieved with a 2.5 inch focus lens providing a focal depth of ≈3 mm and a focus diameter of 170 µm. The center wavelength of the laser was 10.6 ± 0.03 µm. The scanning speed v', generically given in %, was converted into s·m^{-1}. The effective output power P of the laser was measured with a Solo 2 (Gentec Electro-Optics) power meter. The resulting energy input per distance (or fluence) F in J·m^{-1} in the vector mode onto the film is given by

$$F = P \cdot v' \tag{1}$$

For the experiments, the laser settings were adjusted to meet the requirements of the films according to **Table 1**.

2.6. Determination of the Specific Surface Areas

The SSA of LP-NC were determined by the methylene blue (MB) adsorption method.[36–38] LP-NC films in a size of 2 × 1 cm were printed on PET sheets and their masses were determined with a micro-balance. The PET-supported films were then immersed into 6 mL of a 9.5 × 10^{-5} M solution of MB in polypropylene vials and stirred for 24 h. The solutions were centrifuged and the amount of adsorbed MB was determined by measuring the absorbance of the supernatant with respect to a reference solution. An area of 1.35 nm^2 per molecule MB was assumed.

2.7. VOCs Sensing

The sensor platforms were placed in a gas-proof glass flow-cell (V_{cell} ≈ 0.1 L) and their ends were connected to two electrode pins. The electrical characterization was performed with an impedance unit at a frequency of 1000 Hz and a current intensity at 0.05 mA for all measurements. The total flow of nitrogen was set to 1 L·min^{-1}. 30 min cycles between pure nitrogen and a flow containing different contents of acetone were performed. Either 1%, 5%, or 10% of the total flow were passed through a reservoir of the liquid VOCs with a temperature fixed at 30 °C. The final concentration of the analyte was approximated using the ideal gas law based on the vapor pressure of the VOC.[39]

2.8. Characterization

Scanning electron microscopy was performed on a Zeiss LEO 1550-Gemini system (acceleration voltage: 3 to 10 kV). An Oxford Instruments X-MAX 80 mm^2 detector was used to collect the SEM-EDX data. TEM was performed using a double Cs corrected JEOL JEM-ARM200F (S)TEM operated at 80 kV, 10 µA, and equipped with a cold-field emission gun and a high-angle silicon drift EDX detector (solid angle up to 0.98 steradians with a detection area of 100 mm^2). Annular dark field scanning TEM (ADF–STEM) images were collected at a probe convergence semi-angle of 25 mrad. The so-called "beam shower" procedure was performed with a defocused beam at a magnification of 8000× for 30 min. This procedure was necessary for reducing hydrocarbon contamination during subsequent imaging at high magnification. To prepare the TEM samples, the carbon material was dispersed in methanol, sonicated for 10 min, drop cast on a Lacey carbon TEM grid and dried at room temperature. Elemental combustion analysis was performed with a vario MICRO cube CHNOS elemental analyzer (Elementar Analysensysteme GmbH). The elements were detected with a thermal conductivity detector for C, H, N, and O and an IR detector for sulfur. Raman spectra were obtained with a confocal Raman Microscope (alpha300, WITec, Germany) equipped with a piezo-scanner (P-500, Physik Instrumente, Karlsruhe, Germany). The laser, λ = 532 or 785 nm was focused on the samples through a 20× objective. The laser power on the sample was set to 1.0 mW. X-ray diffraction was performed on a Bruker D8 Advance diffractometer in the Bragg-Brentano mode at the Cu Kα wavelength. Impedance measurements were performed on a Solartron 1287 potentiostat in combination with a SI 1260 impedance unit. For frequency measurements, the current was kept constant at 0.1 mA and for current sweeps,

Table 1. Laser parameters used in the experiments to fit the film thickness.

Thickness [µm]	Power [%] (generic)	Power [W]	Speed [%] (generic)	Speed [s m^{-1}]	Fluence [J m^{-1}]
13	1.9	0.97	0.6	98	94.5
19	2.0	1.02	0.6	98	99.5
28	2.1	1.07	0.6	98	104.5
56	2.5	1.27	0.6	98	124.4
70	2.7	1.37	0.6	98	134.3

a frequency of 100 Hz was used. Hall measurements were carried out at room temperature in an Accent HL5500PC using a magnetic strength of 0.3 T. The samples were fabricated in a cloverleaf geometry and the pins contacted the film via indium pads. After checking the ohmic response of the contacts, the measurements for LP-NC(NaI40) were done with the current source set for AC operation under vacuum. The entire Hall measurement was cycled five times to obtain an average value. LP-MoC$_{1-x}$(10)@NC and LP-MoC$_{1-x}$(10)@NC(NaI40) measurements were done in the DC mode. Each measurement was repeated a minimum of four times. XPS was performed with a CISSY station (UHV) with a SPECS XR 50 X ray gun Mg Kα radiation (1254.6 eV) and combined lens analyzer module. The Shirley background deletion was used in photoemission spectra analysis.

3. Results and Discussion

The process of CLaP using organic, molecular precursors has been described in detail in a previous study.[15] First, so-called carbon network forming agents consisting of pre-carbonized molecular precursors were synthesized. To this end, mixtures of citric acid and urea were pyrolyzed in an oven at 300 °C for 2 h under a nitrogen flow to obtain a black powder. This powder is a mixture of carbon-rich nanoparticles and molecular side products.[40] The insoluble carbon-rich nanoparticles particles were separated from the soluble side-products by washing in boiling H$_2$O. The insoluble particles appear agglomerated, with diameters between 50 and 500 nm according to TEM analysis (Figure S1A, Supporting Information). A peak at 27.4° 2Θ in the diffraction pattern (Figure S1B, Supporting Information) corresponds to the typical d-spacing for π-stacked hydrocarbons and is characteristic of the presence of polyaromatic domains within the CNFA. Their formation is confirmed by the presence of broad D- and G-bands at 1355 and 1568 cm^{-1}, respectively, in the Raman spectrum (Figure S1C, Supporting Information).

The CNFA was processed to highly viscous precursor inks (**Figure 1**A). The standard ink is composed of the CNFA, PVP as a FFA, and ethylene glycol (EtGly) as a solvent. Additional components, such as porogens (NaI) and functional additives (AHM) were added to tune the properties of the final LP-NC. The elemental compositions of these precursors are given in Table S1, Supporting Information. From these inks, films

with thicknesses between 15 and 70 μm were prepared by doctor blading on a PET substrate and evaporating the solvent at 80 °C. Then, carbonization was achieved by irradiating the films with a mid-IR CO$_2$-laser with preset patterns (Figure 1B). After laser-treatment, the unexposed precursor film was removed by rinsing with deionized water. The resulting laser-carbonized structures are referred to as LP-NC films. Finally, the films were used as resistive sensor platforms to detect different VOCs in a gas-flow-cell (Figure 1C).

3.1. LP-NC

The SEM image in Figure S2A, Supporting Information shows the typical appearance of an LP-NC film with its foamy morphology composed of the conductive (nitrogen doped-) carbon network with macro and mesopores.[18] These pores evolve during the laser-treatment upon sudden release of gases, such as CO or CO$_2$. The presence of smaller mesopores is also observed by TEM (Figure S2B, Supporting Information).

The original elemental composition of the CNFA is 47 wt% carbon (C), 19 wt% nitrogen (N), and 31 wt% oxygen (O) as determined by elemental combustion analysis. Upon laser-treatment, the overall composition changes to 68 wt% C, 13 wt% N, and 27 wt% O in the collected powders. Noteworthy, the degree of carbonization follows a gradient from the top to the bottom of the film as demonstrated in EDX elemental analysis maps of cross sections of the as-prepared LP-NC films (**Figure 2**A). Clearly, the top of the film is dominated by carbon while large amounts of nitrogen and oxygen are detected toward the bottom of the film. On top of the film, the carbon content reaches 92 wt% C (8 wt% O). In the XRD pattern of the as-prepared LP-NC a broad peak at 2Θ = 26.1° characteristic for graphitic layers is detected (Figure S2C, Supporting Information). The shift toward smaller angles in comparison to the CNFA is attributed to the reduction in nitrogen content and the higher degree of graphitization. The Raman spectrum shows common features of a turbostratic graphitic material showing D, G, and G′ vibration bands localized at 1335, 1573, and 2664 cm^{-1}, respectively (Figure S2D, Supporting Information). The pronounced D band indicates the presence of significant amounts of graphitic defects, such as sp^3-carbon, heteroatoms, or vacancies.

For electronic sorption applications, such as sensors, the electrical conductivity and the SSA are pivotal factors. To tune
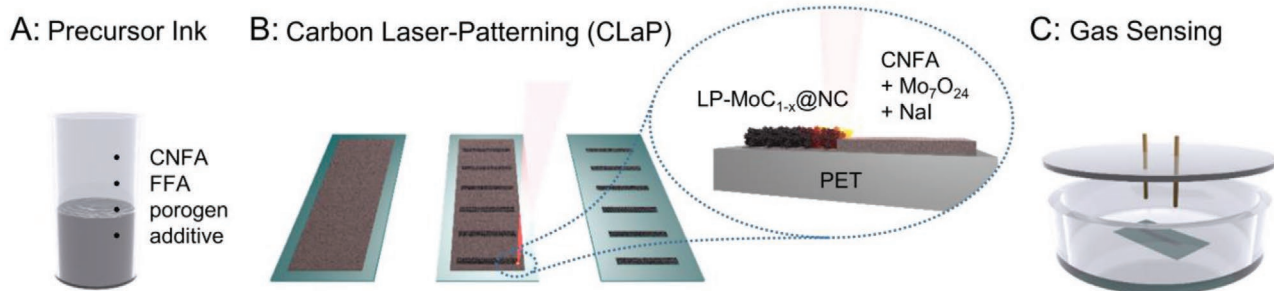

Figure 1. Scheme of the sensor production and measuring process; A) preparation of precursor inks with different compositions including CNFA, FFA, porogens, and additives; B) carbon laser-patterning of precursor films cast on PET and subsequent rinsing with H$_2$O to obtain LP-NC; C) electrochemical gas-sensing cell used to characterize the resistive response of the LP-NC sensor platforms in different environments.
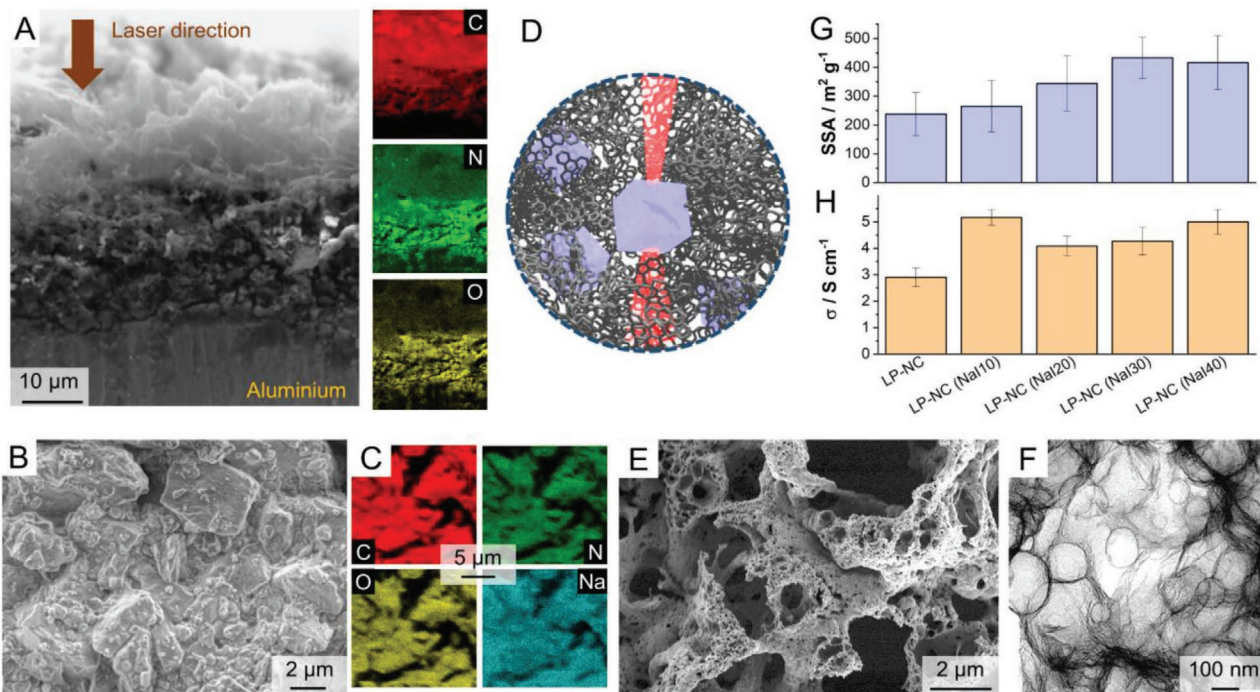
ADVANCED
SCIENCE NEWS
www.advancedsciencenews.com

ADVANCED
FUNCTIONAL
MATERIALS
www.afm-journal.de

Figure 2. A) Scanning electron micrograph of a LP-NC film on an aluminium sheet and corresponding EDX maps showing the qualitative carbon, nitrogen, and oxygen distribution across the film; B) scanning electron micrograph of the CNFA film containing 40 wt% NaI and C) corresponding EDX maps; D) illustration of the alkali halide salt embedded in the CNFA film and their transmittance for IR-laser radiation; E) scanning electron micrograph of LP-NC(NaI40); F) transmission electron micrograph of LP-NC(NaI40). G) Dependence of specific surface area on the amount of NaI added to the CNFA film; H) dependence of sheet conductivity on the amount of NaI added to the CNFA film.

the SSA and, thus, the sorption-sensitivity of the sensor platforms, IR-transparent salts (alkali halides) were added as porogens. Among the typical IR-transparent salts, NaI shows the highest solubility in ethylene glycol, the solvent for the precursor ink. In this study, we focused on NaI only, because the solubility of other salts in ethylene glycol, such as NaCl, KCl, NaBr, and KBr is too low to reach porogeneic activity. Its high solubility in water is also beneficial for the rinsing step after laser-treatment. Different amounts of NaI (10–50 wt% with respect to the CNFA) were added to the precursor inks and their impact on the formation and properties of the LP-NC films were tested. The products are named LP-NC(NaI10)–LP-NC(NaI40). Larger amounts of NaI (>40 wt%) result in delamination of the films. Upon drying, a homogeneous precursor film is formed (Figure 2B). As demonstrated by the EDX maps in Figure 2C, the NaI is uniformly blended into the CNFA film and does not separate or form micro-crystallites. The distributed IR-transparent salt within the film transmits the laser energy and allows effective carbonization of the surrounding CNFA (Figure 2D). After laser-treatment, the films show a uniform porous morphology and SEM analysis does not reveal major differences relative to the reference LP NC (Figure 2E). A representative TEM image in Figure 2F shows a strong resemblance to the reference LP-NC with bubble-like pores caused by the aforementioned laser-induced release of evaporating CNFA.

To quantify the SSAs of the LP-NC(NaI) films, the MB adsorption method was chosen, which is suitable for small quantities (<1 mg) of carbonaceous samples (see Experimental Section). The mass densities of the LP-NC films printed on PET

sheets were determined to be ≈10–50 µg cm^{-2}. PET supported films with defined mass loadings were immersed into aqueous solutions of MB with defined concentrations and stirred for 24 h and the amount of MB adsorbed was determined by UV–vis absorption spectroscopy. Noteworthy, the MB adsorption method typically gives lower SSA values for nitrogen-doped carbons, meaning that the absolute values can be treated as a lower limit for the true SSA. For comparison, a list with other carbon and nitrogen-doped carbon materials is given in Table S2, Supporting Information. The SSAs of the LP-NC was increased from ≈238 to ≈433 m$^2 \cdot$g^{-1} upon adding 30–40 wt% NaI to the precursor ink (Figure 2G). This range is similar to the range found for LIG from polyimides (≈340 m$^2 \cdot$g^{-1}).[41] The increased SSA by a factor of two and the largely unchanged morphological features of the LP-NC upon addition of NaI into the precursor ink confirms its hypothesized role as a porogen. After laser treatment, remaining NaI is removed by thorough rinsing of the film with H$_2$O, which is confirmed by EDX-analysis of the final films (Figure S3, Supporting Information). The Raman spectrum of LP-NC(NaI40) film (Figure S4, Supporting Information) shows a higher D-band compared to bare LP-NC, which indicates that NaI has an effect on the carbonization mechanism.

A statistical electronic analysis of 50 samples of the resulting LP-NC(NaI) films shows that the conductivity is generally higher when NaI was added (Figure 2H). Addition of 10 wt% NaI results in an increase from 2.8 to 5.2 S cm^{-1}. While higher amounts (20–40 wt%) cause a drop in conductivity, the conductivity remains above the reference sample without NaI. The

addition of a salt to the ink supports a better dispersion of the negatively charged CNFA particles due to the Debye–Hückel arrangement in a concentrated electrolyte solution. The Debye length is shortened resulting in an improved dispersion. At concentrations > 20 wt% the effect of NaI as a porogen from NaI crystallites sets in. LP-NC(NaI40) exhibits a positive Hall coefficient of $R_H = +0.19$ cm$^3 \cdot$ C^{-1} indicating an intrinsic p-type semiconducting behavior that is commonly observed for carbonaceous samples carrying oxygen functionalities on their surface.[42,43] Notably, the charge carrier mobility obtained from the Hall measurements of 0.23 cm$^2 \cdot$ (V$\cdot$s)$^{-1}$ for LP-NC(NaI40) is higher than the reference LP-NC (0.12 cm$^2 \cdot$ (V$\cdot$s)$^{-1}$),[18] which is in line with the increased SSA and thus a larger conjugated surface. The higher defect density in LP-NC(NaI40) measured by Raman spectroscopy (Figure S4, Supporting Information) contributes only little to lowering the charge carrier mobility.

As a general scheme, the presence of an IR-laser transparent salt in the precursor films supports the penetration of the laser energy into deeper layers of the precursor film. Subsequently, larger amounts of material are carbonized and contribute to the overall conductivity. The higher value for only 10% NaI may be attributed to a lower porogeneic activity at such low concentrations and a better percolation of the carbon network. 40 wt% of NaI appears to be the best compromise to maximize the porosity, the electronic conductivity and to conserve a good mechanical stability, that is, avoiding delamination or cracking.

3.2. LP-MoC$_{1-x}$@NC

To increase the sensitivity toward different VOCs, the LP-NC was impregnated with MoC$_{1-x}$ nanoparticles. To this end, a molecular molybdenum precursor was added to the ink in addition to the CNFA, the FFA, and the porogen. A negatively charged complex, AHM, was chosen to avoid flocculation in the precursor ink since the CNFA, CA/U(300), has a negative ζ-potential of -53 mV.[15] Rapid heating in the laser spot initiates the AHM decomposition and the nucleation of molybdenum carbide (MoC$_{1-x}$) nanoparticles.

First, we tested the influence of the AHM content on the electronic properties of the final laser-patterned films, denoted as LP-MoC$_{1-x}$(wt%)@NC (**Figure 3**A). Addition of 1 wt% AHM with respect the mass of CNFA, results in a drop in conductivity from 2.9 to 1.0 S cm^{-1}. Higher amounts of AHM, 5 or 10 wt%, cause the conductivity to increase again to 2.2 or 3.2 S cm^{-1}. The films containing 20 wt% appear brittle and crack easily resulting in low conductivity and very high errors. The SSA remains largely unchanged (Figure S5, Supporting Information).

The MoC$_{1-x}$ nanoparticle impregnated LP-NC produced with 10 wt% of AHM in the precursor ink, here referred to as LP-MoC$_{1-x}$(10)@NC was intensively characterized, as 10% of AHM appears to be the optimum content to preserve the mechanical stability and maximize the electronic conductivity. To determine the molybdenum content, the sample was
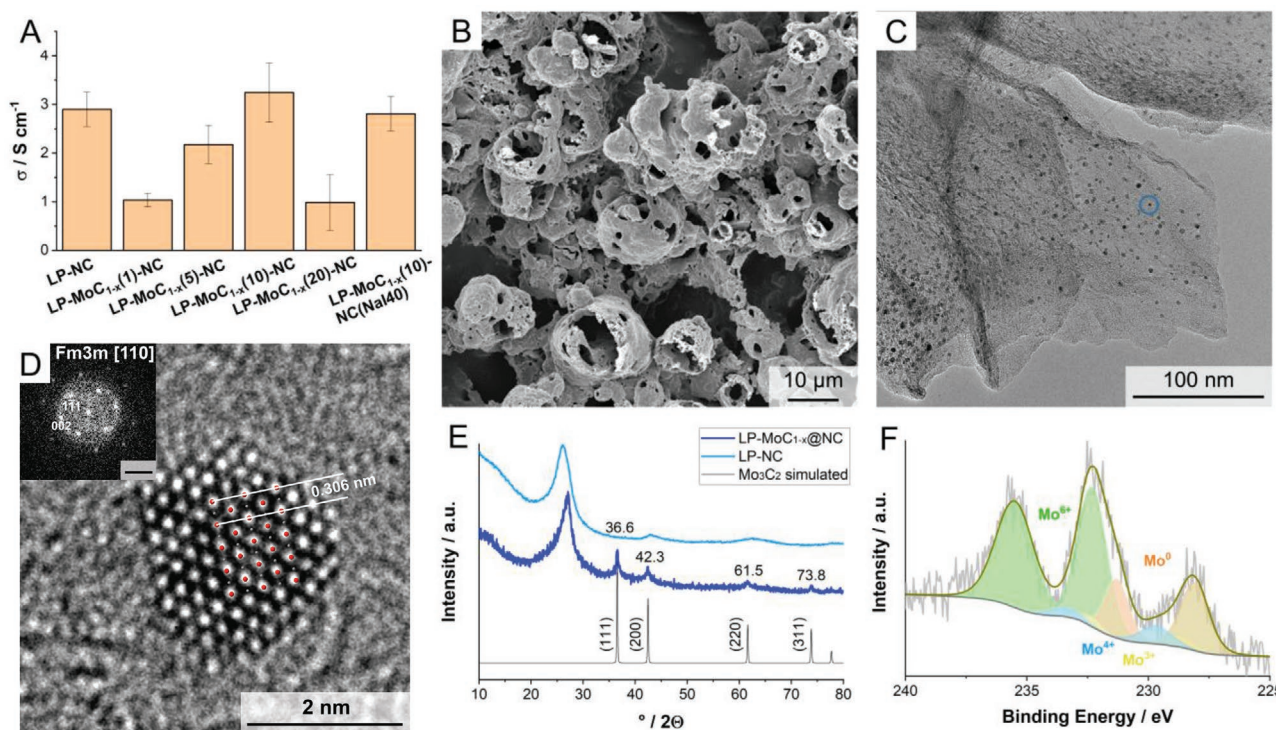

Figure 3. A) Electrical sheet conductivity of LP-MoC$_{1-x}$@NC with different amounts of AHM in the inks; B) scanning electron micrograph of LP-MoC$_{1-x}$(10)@NC showing a foam-like morphology; C) transmission electron microscopy image of LP-MoC$_{1-x}$(10)@NC. D) High-resolution transmission electron image of the particle indicated by the blue circle in (C). The overlapping atoms demonstrate the locations of Mo (red) and C (grey) in the crystal. The inset in (D) shows the corresponding fast Fourier transform indexed in a cubic unit cell, sp.gr. $Fm\bar{3}m$. The scale bar is 5 nm^{-1}. E) X-ray powder diffraction patterns of LP-NC and LP-MoC$_{1-x}$(10)@NC, respectively, and the simulated pattern of Mo$_3$C$_2$; F) X-ray photoelectron spectrograph of the Mo$_{3d}$ core level of LP-MoC$_{1-x}$(10)@NC.

analyzed by inductively coupled plasma mass spectrometry. After laser-treatment the overall Mo content is 12.9 wt% in LP-MoC$_{1-x}$(10)@NC. The higher Mo content in comparison to the precursor ink (4.28 wt%) shows that the CNFA evaporates more than the Mo precursor (AHM) during the laser-carbonization. The overall foamy morphology of the LP-MoC$_{1-x}$(10)@NC films is, in principle, the same as for LP-NC (Figure 3B) and macroscopic features, such as thickness and appearance, are not altered. The size range of the MoC$_{1-x}$ nanoparticles as observed in the TEM images in Figure 3C is between 2 and 20 nanometers (Figure S6, Supporting Information).

Fast Fourier transformed HRTEM images of the particles can be indexed in the cubic lattice with the unit cell parameter $a =$ 4.15(4) Å, sp.gr. $Fm\overline{3}m$, and can be described with the NaCl-structure type typical for MoC$_{1-x}$ solid solution (Figure 3C,D).[44] Furthermore, the EDX spectra and the STEM-EDXS maps (Figure S7, Supporting Information) of the LP-MoC$_{1-x}$(10)@NC sample show the presence of Mo, C, N, and O, whereas the carbon network spectra only show N and O signals, confirming the formation of molybdenum carbide particles. The XRD pattern in Figure 3E shows the presence of a graphitic peak at 27° 2Θ, similar to that found for LP-NC, while all other peaks can be attributed to cubic MoC$_{1-x}$ with the unit cell parameter $a =$ 4.253(5) Å.[45] Discrepancies in the unit cell parameters obtained from either FFT or XRD can be explained by both, much lower accuracy of the lattice space determination of the HRTEM-FFT analysis and much lower statistics than in case of XRD.

The Mo$_{3d}$ XPS core level spectrum in Figure 3F shows the presence of Mo in the oxidation states Mo^0, Mo^{3+}, Mo^{4+}, and Mo^{6+}. The most prominent are Mo^0 at 228.1 (3d$_{5/2}$) and 231.3 eV (3d$_{3/2}$), and Mo^{6+} at 232.3 (3d$_{5/2}$) and 235.5 eV (3d$_{3/2}$). Minor signals at 228.8 (3d$_{5/2}$) and 232.4 eV(3d$_{3/2}$) and at 229.7 (3d$_{5/2}$) and 233.4 eV (3d$_{3/2}$) are attributed to Mo^{3+} and Mo^{4+}, respectively. This oxidation pattern, especially the presence of Mo^0 is typical for MoC$_{1-x}$ or MoC.[46] The fitting data of the C$_{1s}$, N$_{1s}$, and O$_{1s}$ regions are presented in Figure S8, Supporting Information.

The Raman spectrum of LP-MoC$_{1-x}$(10)@NC shows sharp D- and G-bands, although the peaks appear much broader and the D-band significantly more intense, relative to LP NC (Figure S9, Supporting Information). The shape and intensity of the 2D band are correlated with the degree of stacking of graphitized domains within the material. Carbon in the amorphous state shows only a low intensity 2D band.[47] At the same time, the D-band, which is correlated to the amount of sp^2-defects is significantly increased. Therefore, we infer a lower degree of stacking due to the presence of MoC$_{1-x}$ nanoparticles and a higher number of defects. From these observations, we deduce that the MoC$_{1-x}$ nanoparticles are not only grown on the surface but also incorporated into the LP-NC network. The size distribution of the MoC$_{1-x}$ nanoparticles is not affected by the presence of NaI during the laser-induced reaction (Figure S1, Supporting Information). As shown in the cross-sectional EDX maps of 70 μm thick LP-MoC$_{1-x}$(10)@NC(NaI40) films, the MoC$_{1-x}$ nanoparticles are uniformly distributed across the film (Figure S11, Supporting Information).

The formation of MoC$_{1-x}$ nanoparticles occurs in situ during the laser-induced carbonization. A commonly accepted mechanism is the reduction of transient molybdenum clusters to molybdenum carbides by carbothermal reduction.[48] High carbon content and high temperatures (>1500 °C) in the laser spot facilitate the formation of MoC$_{1-x}$.[49] The presence of nanometer-sized graphitic domains surrounding the MoC$_{1-x}$ nanoparticles are confirmed by high-resolution STEM images shown in Figure S12, Supporting Information. The meso/macroscopic morphology of the LP-MoC$_{1-x}$(10)@NC is not significantly affected by the presence of AHM in the precursor ink. However, the electronic properties (i.e., electrical conductivity) are impaired, with the drop in conductivity upon adding small amounts of AHM (<10 wt%) consistent with perturbation due to the increased number of defects in the LP-NC network. Larger amounts of AHM support the nucleation of metallic MoC$_{1-x}$ nanoparticles, which contribute positively to the overall conductivity. Hall measurements yielded a positive coefficient also for LP-MoC$_{1-x}$(10)@NC of $R_H = +0.32$ cm$^3 \cdot$C^{-1}. The charge carrier density is slightly lower with 1.96×10^{19} cm^{-3} than the LP-NC sample, while the charge carrier mobility is higher with 1.42 cm$^2 \cdot$(V·s)$^{-1}$ (Table S3, Supporting Information). These electronic properties are affected by the addition of NaI. The Hall coefficient, $R_H = +2.67$ cm$^3 \cdot$C^{-1}, is significantly higher than LP-MoC$_{1-x}$@NC, due to a threefold increase in charge carrier mobility to 4.35 cm$^2 \cdot$(V·s)$^{-1}$ and lower charge carrier density of 2.34×10^{18} cm^{-3}.

3.3. VOC Sensing

Finally, we tested films of the optimized materials, LP-NC(NaI40), LP-MoC$_{1-x}$(10)@NC, and LP-MoC$_{1-x}$(10)@NC(Na40), as sensor platforms for resistive sensing of VOCs. In every production step, several sensor platforms were printed consecutively into one film (**Figure 4**A). A standard sensor pattern is made of five parallel laser lines of 5 mm in length distributed across a width of ≈0.5 mm (Figure 4B). This simple geometry allows for the direct comparison of the materials properties, while geometric effects are neglected. For each measurement, a sensor platform was placed into a gas-flow-cell and the two ends of the sensor platform were connected by electrodes to measure the impedance in a four-probe arrangement. The gas composition inside the cell was controlled by two parallel connected mass-flow controllers to ensure a constant gas flow with compositions of 0.5–10% target gas in a carrier gas (N$_2$ or air) atmosphere. A prominent biomarker, namely acetone, was chosen as the primary target gas.[50]

First, we tested the effect of film thickness on acetone sensitivity, using the LP-MoC$_{1-x}$(10)@NC sensor as a representative platform (Figure S13, Supporting Information). The best results for this sensor were achieved with a thickness of 70 μm, so we utilized this thickness range for additional tests. Thicker films tend to delaminate during the rinsing step. Notably, for films thinner than 19 μm a weak positive response, that is, an increase of resistivity upon exposure to acetone is detected, which is attributed to a lower degree of graphitization and higher defect density in the laser-patterned carbon.

The resistivity response of LP-NC(NaI40) upon exposure to 2.5% acetone is $\Delta R/R_0 = 2.7\%$ and a similar value of $\Delta R/R_0 = 3.0\%$ is detected for the non-porogen-containing
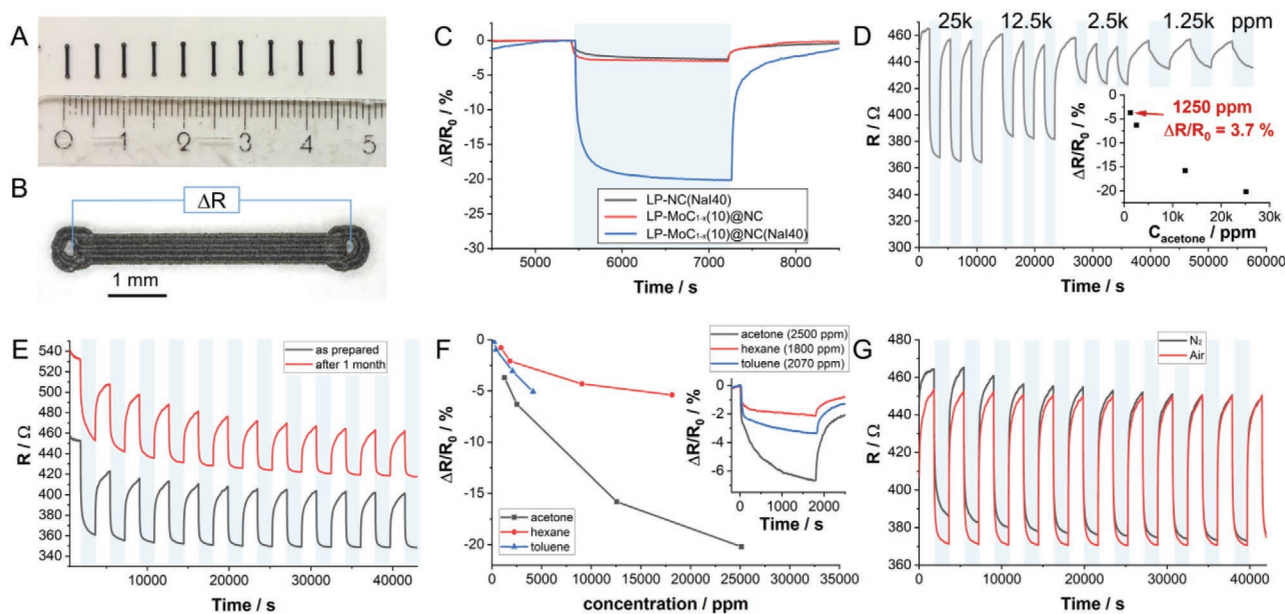
**ADVANCED
SCIENCE NEWS**

www.advancedsciencenews.com

**ADVANCED
FUNCTIONAL
MATERIALS**

www.afm-journal.de

Figure 4. A) Photograph of a set of sensor platforms obtained by carbon laser-patterning on PET; B) optical micrograph showing the dimensions of the sensor-platform used for resistive gas-sensing experiments; C) response of the sensor materials LP-NC(NaI40), LP-MoC$_{1-x}$(10)@NC, and LP-MoC$_{1-x}$(10)@NC(NaI40) upon exposure to 2.5% acetone; D) resistive response of LP-MoC$_{1-x}$(10)@NC(NaI40) toward exposure to different concentrations of acetone; E) resistive response of LP-MoC$_{1-x}$(10)@NC(NaI40) after 1 month in comparison to a freshly prepared sensor platform; F) comparison of the resistive response of LP-MoC$_{1-x}$(10)@NC(NaI40) toward different concentrations of acetone (black), hexane (red), and toluene (blue); G) resistive response of LP- LP-MoC$_{1-x}$(10)@NC(NaI40) toward 2.5% of acetone using N$_2$ (black) or dry air (red) as carrier gas.

LP-MoC$_{1-x}$(10)@NC (Figure 4C). In LP-MoC$_{1-x}$(10)@NC(NaI40) the response is drastically increased by more than a factor of six giving $\Delta R/R_0 = 20.2\%$ for 2.5% acetone. The response depends on the analyte concentration as shown in Figure 4D and a reasonable response of $\Delta R/R_0 = 3.7\%$ at relatively low analyte concentrations of 1250 ppm acetone is detected.

Next, we tested the long-term stability of the sensor platforms. To this end, the sensor platform was stored under ambient conditions for 1 month and tested under the same conditions for sensing acetone (2.5%). With respect to the freshly prepared sample, the aged sample shows a slightly lower response of $\Delta R/R_0 = 15.8\%$ (Figure 4E). The reduced overall conductivity is attributed to a partial oxidation/degradation of the surface groups on the LP-MoC$_{1-x}$@NC(NaI40).

As shown in the materials characterization section and previous studies, the surface of LP-NC and LP-MoC$_{1-x}$@NC(NaI40) is largely oxygenated.[51] Such oxygen-containing functional groups cause the surface to be preferentially susceptible to polar analytes, which is supported by the data shown in Figure 4F. The response toward polar acetone is significantly higher than to non-polar analytes such as hexane or toluene. The higher response to toluene in contrast to hexane is likely due to their attractive π–π interactions with π-conjugated domains on the surface of LP-MoC$_{1-x}$@NC(NaI40).

The typical sensing mechanism for acetone with semiconductor materials like metal oxides or graphene composites is proposed to stem from the interaction with ionosorbed oxygen.[52] Before any sensor experiments, in the initial state, oxygen from the atmosphere is adsorbed and reduced to oxygen anions like O_2^-, O^-, or O^{2-} on the semiconductor surface resulting in a decrease of the electron density in the composite

material. In presence of acetone, these oxygen anions react to form CO_2 resulting in an increase of the electronic density of the semiconductor.[6,53,54] However, this mechanism requires the supply of oxygen during operation and high operating temperatures. In our experiments we used either nitrogen or dry air as carrier gases (Figure 4G). The response in terms of resistivity change in both media is the same. Moreover, the response time and the recovery time during acetone cycling are similar in both carrier gases. This indicates that the presence of O_2 does not influence the sensing behavior, as the effect on the electronic properties during acetone exposure is negligible. Therefore, we conclude that the change in resistance is dominated by electronic sensitization effects rather than chemical, that is, physisorption of gaseous acetone onto the surface of the LP-MoC$_{1-x}$(10)@NC(NaI40) and the subsequent modulation of the depletion regions.[55]

Considering these observations, our laser-patterned composite material shows intriguing performance in room temperature sensing of VOCs. Reliable room temperature sensing of VOCs using simple resistive architectures based on carbon is a challenge due to difficulties in processing and stability. Although many conventional sensing materials like metal oxides show a higher sensitivity at room temperature, their production and processing is rather tedious requiring deposition on interdigitated gold electrodes.[56,57] In comparison to other carbon and graphene based materials the performance of LP-MoC$_{1-x}$(10)@NC(NaI40) is competitive.[58–60] For example, multi-walled carbon nanotubes as p-type semiconductor show a response of ≈0.4% to 15 ppm acetone at room temperature.[33] Reduced graphene oxide is often used as a conductive sensing platform showing $\Delta R/R_0$ values of ≈1%

**ADVANCED
SCIENCE NEWS**
www.advancedsciencenews.com

**ADVANCED
FUNCTIONAL
MATERIALS**
www.afm-journal.de

upon exposure to ≈500–1000 ppm of different alcohols at room temperature.[34,35]

Generally, in carbonaceous materials, the active sites involved in the sensing mechanisms are presumed to be defects in the graphitic structure, such as vacancies or oxygen functional groups.[61] According to elemental analysis, Raman, and XRD, the conductive carbonized part of the LP-NC is composed of highly defective, porous, and oxygenated turbostratic carbon. Its defective nature makes the surface rather polar with a high intrinsic binding affinity to polar analytes. In contrast to graphene with a largely unperturbed π-surface, the surface of LP-NC is not expected to be more sensitive with chemisorbed oxygen.

Taking these aspects into consideration the LP-NC sensor material differs from graphene. Due to its intrinsically oxygenated surface, LP-NC acts as a p-type semiconductor,[18] which is confirmed by positive Hall coefficients mentioned above. Upon interaction of the surface defects or functional groups with the analytes, the charge carrier density within the LP-NC increases which is reflected in an increase in conductivity.[53]

A common approach to increase the sensitivity of carbon materials is the integration of Schottky or heterojunctions,[62] e.g., between carbon nanotubes and Au nanoparticles. These show response of $\Delta R/R_0 = 4.6\%$ to 800 ppm acetone.[63]

By introduction of MoC_{1-x} nanoparticles into the LP-NC, nanoscale grain boundaries are created between the metallic MoC_{1-x} and the semiconducting LP-NC. These cause the formation of Schottky junctions and thus depletion zones around the nanoparticles (**Figure 5**). According to the Mott-theory, p-type semiconductors form rectifying contacts to metals of work function lower than that of the semiconductor, that is, $\Phi_M < \Phi_S$ and ohmic contacts for $\Phi_M > \Phi_S$. The work function of MoC_{1-x} solid solution is difficult to determine experimentally. The work functions of metal carbides are highly dependent on the phase, the crystal facet, and the type of termination. For example, the theoretically determined work functions of MoC or Mo_2C range between 3.4 and 7.5 eV.[64–66] Given the polydisperse nature of MoC_{1-x} incorporated into LP-NC, different facets and compositions are exposed to the surrounding carbon. LP-NC is best compared with amorphous or poly-crystalline carbons, such as MWCNTs or carbon black. Their work functions are typically ≈4.5 ± 0.3 eV.[67–69]

In the present case, the MoC_{1-x} nanoparticles accumulate charge carriers and create doping-sensitive zones. Acetone as a closed shell molecule is expected to interact with the LP-NC surface by formation or enhancement of dipoles on the surface which induce a charge modulation within the doping-sensitive grain boundaries.[70,71] Therefore, the higher sensing response in LP-MoC_{1-x}(10)@NC(NaI40) is explained by the lower charge carrier density in the overall material and the increased SSA.

This is the first example of a molecule-based laser-patterned resistive carbon sensor based on direct interactions with the target gas and the in situ incorporation of metal nanoparticles. Synthetically and environmentally, this method displays an advantage over LIG from polyimides, which have shown great promise as sensing platforms after post-functionalization with nanoparticles.[72–76] Conceptually, they are different in terms of morphology and detection mechanisms. For
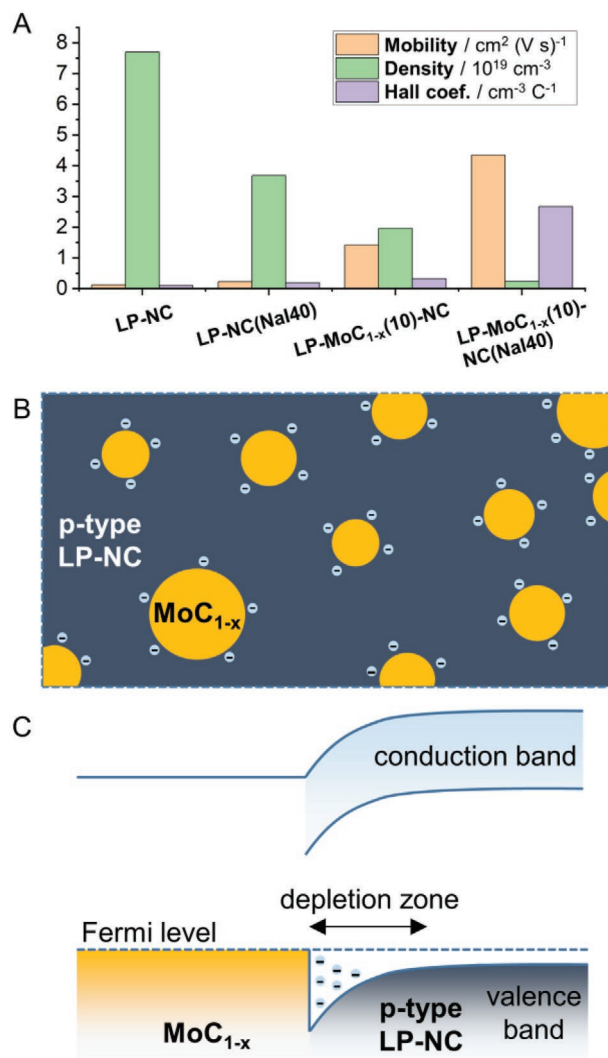

Figure 5. A) Comparison of the charge carrier mobilities, densities, and Hall coefficients of the four tested samples obtained by Hall measurements. B) Illustration of the charge accumulation by MoC_{1-x} nanoparticles embedded into a conductive p-type LP-NC network; C) corresponding band-diagram illustrating the depletion zones created around the MoC_{1-x} nanoparticles (1 column).

example, LIGs have shown a high response to different gases versus vacuum as a response to the different thermal conductivities of the respective gases.[12] In other concepts, laser-patterned resistive carbons are used as transducer platforms for functionalization with selective bio-receptors.[8] In our LP-NC and their nano-composites, we observe several effects simultaneously. On the one hand, we have a highly defective carbon, which allows an intrinsic room-temperature sensitivity toward different target gases. On the other hand, the uniform impregnation of MoC_{1-x} nanoparticles forms overlapping doping sensitive Schottky-junctions. Indeed, it has been shown, for example, that the particle size of certain materials and the subsequent generation of converging Schottky barriers lead to drastic increases in sensitivity.[77–79] Their exact synergetic effects are yet to be explored in future studies on the detailed sensing mechanism.

4. Conclusions

In this study, we demonstrated the applicability of CLaP for resistive sensing of VOCs. CLaP is an interesting new tool for the fast and precise large-scale production of patterned carbonized films with different compositions for sensor arrays. The use of molecular starting materials enables wide possibilities for tuning the compositional and electronic properties of the obtained films. This study presents first insights into how the materials properties can be tuned to increase the sensitivity toward different analytes.

The specific surface area of the LP-NC was increased by addition of an IR-laser-transparent alkali halide salt—sodium iodide—into the precursor inks. Moreover, the fast speed of the laser-induced reaction allows for the in situ synthesis of small and uniform MoC_{1-x} nanoparticles with sizes < 10 nm achieved by the simple selective addition of soluble precursors to the precursor ink. The thus created Schottky junctions at the nanoscale grain boundaries between MoC_{1-x} and the conductive carbon network further decrease the charge carrier density whereby the sensitivity of the LP-NC films toward acetone was drastically increased.

The room-temperature sensing operation of the MoC_{1-x} nanoparticle impregnated LP-NCs is stable and reproducible and shows a remarkable long-term stability. However, to detect concentrations of analytes on the order of parts per billion improvements in the materials structure are necessary. Alternative porogens to further increase the surface area or tune the pore properties to facilitate bulk interactions with target gases rather than outer surface only may be a possible solution. Moreover, for mobile application under ambient conditions and different relative humidities, concepts for the selectivity toward different analytes, for example, tuning the graphitization degree, have to be studied. Further targets of future studies will be miniaturization and optimization of the platform geometries as the sizes of the obtained sensor platforms are limited by the resolution of the laser and the grain size of the agglomerated precursor particles. The CLaP method, in principle, allows for the simple incorporation of different kinds of nanoparticles of tunable sizes, which is a good foundation for systematic studies on the interplay between nanoparticles and their impact on their sensing properties toward different analytes.

Supporting Information

Supporting Information is available from the Wiley Online Library or from the author.

Conflict of Interest

The authors declare no conflict of interest.

Data Availability Statement

Research data are not shared.

[1] T. M. Swager, K. A. Mirica, *Chem. Rev.* **2019**, *119*, 1.

[2] B. Ciui, A. Martin, R. K. Mishra, T. Nakagawa, T. J. Dawkins, M. Lyu, C. Cristea, R. Sandulescu, J. Wang, *ACS Sens.* **2018**, *3*, 2375.

[3] N. Wongkaew, M. Simsek, C. Griesche, A. J. Baeumner, *Chem. Rev.* **2019**, *119*, 120.

[4] C. Mackin, A. Fasoli, M. Xue, Y. Lin, A. Adebiyi, L. Bozano, T. Palacios, *2D Mater.* **2020**, *7*, 022002.

[5] M. E. Franke, T. J. Koplin, U. Simon, *Small* **2006**, *2*, 36.

[6] H. G. Moon, Y. Jung, B. Shin, Y. G. Song, J. H. Kim, T. Lee, S. Lee, S. C. Jun, R. B. Kaner, C. Kang, C. Kim, *Adv. Sci.* **2020**, *7*, 2002014.

[7] M. G. Campbell, S. F. Liu, T. M. Swager, M. Dincă, *J. Am. Chem. Soc.* **2015**, *137*, 13780.

[8] L. Huang, J. Su, Y. Song, R. Ye, *Nano-Micro Lett.* **2020**, *12*, 157.

[9] C. Zhu, L.-Q. Tao, Y. Wang, K. Zheng, J. Yu, X. L, X. Chen, Y. Huang, *Sens. Actuators, B* **2020**, *325*, 128790.

[10] A. Watanabe, J. Cai, S. Ogawa, E. Aoyagi, S. Ito, in *Laser-Based Micro- and Nanoprocessing XIII* (Eds: U. Klotzbach, R. Kling, A. Watanabe), SPIE, Bellingham **2019**, p. 38.

[11] S. Sharma, S. K. Ganeshan, P. K. Pattnaik, S. Kanungo, K. N. Chappanda, *Mater. Lett.* **2020**, *262*, 127150.

[12] M. G. Stanford, K. Yang, Y. Chyan, C. Kittrell, J. M. Tour, *ACS Nano* **2019**, *13*, 3474.

[13] V. Strauss, M. Anderson, C. Wang, A. Borenstein, R. B. Kaner, *Small* **2018**, *14*, 1803656.

[14] V. Strauss, M. Anderson, C. L. Turner, R. B. Kaner, *Mater. Today Energy* **2019**, *11*, 114.

[15] S. Delacroix, H. Wang, T. Heil, V. Strauss, *Adv. Electron. Mater.* **2020**, *6*, 2000463.

[16] J. P. Paraknowitsch, J. Zhang, D. Su, A. Thomas, M. Antonietti, *Adv. Mater.* **2010**, *22*, 87.

[17] J. Pampel, A. Mehmood, M. Antonietti, T.-P. Fellinger, *Mater. Horiz.* **2017**, *4*, 493.

[18] S. Delacroix, A. Zieleniewska, A. Ferguson, J. L. Blackburn, S. Ronneberger, F. Löffler, V. Strauss, *ACS Appl. Electron. Mater.* **2020**, *2*, 4146.

**ADVANCED
SCIENCE NEWS**

www.advancedsciencenews.com

**ADVANCED
FUNCTIONAL
MATERIALS**

www.afm-journal.de

[19] S. A. Shafiee, S. C. Perry, H. H. Hamzah, M. M. Mahat, F. A. Al-lolage, M. Z. Ramli, *Electrochem. Commun.* **2020**, *120*, 106828.

[20] S. A. Rasaki, B. Zhang, K. Anbalgam, T. Thomas, M. Yang, *Prog. Solid State Chem.* **2018**, *50*, 1.

[21] W.-F. Chen, J. T. Muckerman, E. Fujita, *Chem. Commun.* **2013**, *49*, 8896.

[22] T. Niu, *Nano Today* **2018**, *18*, 12.

[23] Y. Deng, Y. Ge, M. Xu, Q. Yu, D. Xiao, S. Yao, D. Ma, *Acc. Chem. Res.* **2019**, *52*, 3372.

[24] Y. Ma, G. Guan, X. Hao, J. Cao, A. Abudula, *Renewable Sustainable Energy Rev.* **2017**, *75*, 1101.

[25] D. Geng, M. Li, X. Bo, L. Guo, *Sens. Actuators, B* **2016**, *237*, 581.

[26] K. Hantanasirisakul, Y. Gogotsi, *Adv. Mater.* **2018**, *30*, 1804779.

[27] C. Giordano, C. Erpen, W. Yao, M. Antonietti, *Nano Lett.* **2008**, *8*, 4659.

[28] J. G. Howalt, T. Vegge, *Phys. Chem. Chem. Phys.* **2013**, *15*, 20957.

[29] L. Ma, L. R. L. Ting, V. Molinari, C. Giordano, B. S. Yeo, *J. Mater. Chem. A* **2015**, *3*, 8361.

[30] X. Zang, C. Shen, Y. Chu, B. Li, M. Wei, J. Zhong, M. Sanghadasa, L. Lin, *Adv. Mater.* **2018**, *30*, 1800062.

[31] M. Abou Hamdan, A. Nassereddine, R. Checa, M. Jahjah, C. Pinel, L. Piccolo, N. Perret, *Front. Chem.* **2020**, *8*, 452.

[32] Y. Liu, G. Yu, G.-D. Li, Y. Sun, T. Asefa, W. Chen, X. Zou, *Angew. Chem., Int. Ed.* **2015**, *54*, 10752.

[33] I. Hafaiedh, W. Elleuch, P. Clement, E. Llobet, A. Abdelghani, *Sens. Actuators, B* **2013**, *182*, 344.

[34] A. Lipatov, A. Varezhnikov, P. Wilson, V. Sysoev, A. Kolmakov, A. Sinitskii, *Nanoscale* **2013**, *5*, 5426.

[35] R. Kumar, R. Ghosh, *Sens. Bio-Sens. Res.* **2020**, *28*, 100336.

[36] S. Naeem, V. Baheti, J. Wiener, J. Marek, *J. Text. Inst.* **2017**, *108*, 803.

[37] M. Rafatullah, O. Sulaiman, R. Hashim, A. Ahmad, *J. Hazard. Mater.* **2010**, *177*, 70.

[38] P. T. Hang, *Clays Clay Miner.* **1970**, *18*, 203.

[39] Y. Li, T. Täffner, M. Bischoff, B. Niemeyer, *Int. J. Chem. Eng.* **2012**, *2012*, 417029.

[40] V. Strauss, H. Wang, S. Delacroix, M. Ledendecker, P. Wessig, *Chem. Sci.* **2020**, *11*, 8256.

[41] J. Lin, Z. Peng, Y. Liu, F. Ruiz-Zepeda, R. Ye, E. L. G. Samuel, M. J. Yacaman, B. I. Yakobson, J. M. Tour, *Nat. Commun.* **2014**, *5*, 5714.

[42] P. Esquinazi, J. Krüger, J. Barzola-Quiquia, R. Schönemann, T. Herrmannsdörfer, N. García, *AIP Adv.* **2014**, *4*, 117121.

[43] N. D. K. Tu, J. A. Lim, H. Kim, *Carbon* **2017**, *117*, 447.

[44] B. Granier, J.-M. Badie, F. Almeida Costa Oliveira, T. Magalhães, N. Shohoji, L. Guerra Rosa, J. Cruz Fernandes, *Mater. Trans.* **2008**, *49*, 2673.

[45] K. Oshikawa, M. Nagai, S. Omi, *J. Phys. Chem. B* **2001**, *105*, 9124.

[46] [42]

[47] D. B. Schuepfer, F. Badaczewski, J. M. Guerra-Castro, D. M. Hofmann, C. Heiliger, B. Smarsly, P. J. Klar, *Carbon* **2020**, *161*, 359.

[48] C.-M. Song, W.-C. Cao, C.-Y. Bu, K. He, G.-H. Zhang, *J. Aust. Ceram. Soc.* **2020**, *56*, 1333.

[49] B. Predel, in *B-Ba–C-Zr*, Springer-Verlag, Berlin/Heidelberg **1992**, p. 1.

[50] K. M. Tripathi, T. Y. Kim, D. Losic, T. T. Tung, *Carbon* **2016**, *110*, 97.

[51] H. Wang, S. Delacroix, O. Osswald, M. Anderson, T. Heil, E. Lepre, N. Lopez-Salas, R. B. Kaner, B. Smarsly, V. Strauss, *Carbon* **2021**, *176*, 500.

[52] D. Zhang, A. Liu, H. Chang, B. Xia, *RSC Adv.* **2015**, *5*, 3016.

[53] P. Sun, Y. Cai, S. Du, X. Xu, L. You, J. Ma, F. Liu, X. Liang, Y. Sun, G. Lu, *Sens. Actuators, B* **2013**, *182*, 336.

[54] F. Liu, X. Chu, Y. Dong, W. Zhang, W. Sun, L. Shen, *Sens. Actuators, B* **2013**, *188*, 469.

[55] T. Hussain, M. Sajjad, D. Singh, H. Bae, H. Lee, J. A. Larsson, R. Ahuja, A. Karton, *Carbon* **2020**, *163*, 213.

[56] S. Shao, H. Wu, S. Wang, Q. Hong, R. Koehn, T. Wu, W.-F. Rao, *J. Mater. Chem. C* **2015**, *3*, 10819.

[57] H. Liu, Y. Guo, R. Xie, T. Peng, G. Ma, Y. Tang, *Sens. Actuators, B* **2017**, *246*, 164.

[58] B. Liu, Y. Huang, K. W. Kam, W.-F. Cheung, N. Zhao, B. Zheng, *Biosens. Bioelectron.: X* **2019**, *1*, 100016.

[59] M. Rodner, D. Puglisi, S. Ekeroth, U. Helmersson, I. Shtepliuk, R. Yakimova, K. Uvdal, A. Schütze, J. Eriksson, *Sensors* **2019**, *19*, 918.

[60] C.-M. Yang, T.-C. Chen, Y.-C. Yang, M. Meyyappan, C.-S. Lai, *Sens. Actuators, B* **2017**, *253*, 77.

[61] D. J. Buckley, N. C. G. Black, E. G. Castanon, C. Melios, M. Hardman, O. Kazakova, *2D Mater.* **2020**, *7*, 032002.

[62] A. Di Bartolomeo, *Phys. Rep.* **2016**, *606*, 1.

[63] S. J. Young, Z. D. Lin, *Microsyst. Technol.* **2018**, *24*, 3973.

[64] H. W. Hugosson, O. Eriksson, U. Jansson, A. V. Ruban, P. Souvatzis, I. A. Abrikosov, *Surf. Sci.* **2004**, *557*, 243.

[65] J. R. dos Santos Politi, F. Viñes, J. A. Rodriguez, F. Illas, *Phys. Chem. Chem. Phys.* **2013**, *15*, 12617.

[66] A. A. Rouse, J. B. Bernhard, E. D. Sosa, D. E. Golden, *Appl. Phys. Lett.* **2000**, *76*, 2583.

[67] W. S. Su, T. C. Leung, C. T. Chan, *Phys. Rev. B* **2007**, *76*, 235413.

[68] T. Fabish, M. Hair, *J. Colloid Interface Sci.* **1977**, *62*, 16.

[69] H. F. Ivey, *Phys. Rev.* **1949**, *76*, 567.

[70] A. V. Singhal, H. Charaya, I. Lahiri, *Crit. Rev. Solid State Mater. Sci.* **2017**, *42*, 499.

[71] T. O. Wehling, M. I. Katsnelson, A. I. Lichtenstein, *Chem. Phys. Lett.* **2009**, *476*, 125.

[72] J. Zhu, M. Cho, Y. Li, I. Cho, J.-H. Suh, D. Del Orbe, Y. Jeong, T.-L. Ren, I. Park, *ACS Appl. Mater. Interfaces* **2019**, *11*, 24386.

[73] R. Ye, Z. Peng, T. Wang, Y. Xu, J. Zhang, Y. Li, L. G. Nilewski, J. Lin, J. M. Tour, *ACS Nano* **2015**, *9*, 9244.

[74] J. Zhang, M. Ren, Y. Li, J. M. Tour, *ACS Energy Lett.* **2018**, *3*, 677.

[75] M. Ren, J. Zhang, J. M. Tour, *ACS Appl. Energy Mater.* **2019**, *2*, 1460.

[76] J. Zhang, C. Zhang, J. Sha, H. Fei, Y. Li, J. M. Tour, *ACS Appl. Mater. Interfaces* **2017**, *9*, 26840.

[77] Z. Ansari, S. Ansari, T. Ko, J.-H. Oh, *Sens. Actuators, B* **2002**, *87*, 105.

[78] F. Lu, Y. Liu, M. Dong, X. Wang, *Sens. Actuators, B* **2000**, *66*, 225.

[79] C. Xu, J. Tamaki, N. Miura, N. Yamazoe, *Sens. Actuators, B* **1991**, *3*, 147.